

Some insights of spectral optimization in ocean color inversion

Zhongping Lee^{*a}, Bryan Franz^b, Shaoling Shang^c, Qiang Dong^d, Robert Arnone^e

^aEnvironmental Earth and Ocean Sciences, University of Massachusetts at Boston, 100 Morrissey Blvd, Boston, MA 02125, Zhongping.Lee@umb.edu

^bNASA Goddard Space Flight Center, Greenbelt, MD, 20771

^cState Key Laboratory of Marine Environmental Science, Xiamen University, 361005, China

^dGeosystems Research Institute, Mississippi State University, Stennis Space Center, MS 39529

^eNaval Research Laboratory, Stennis Space Center, MS 39529

ABSTRACT

In the past few decades, various algorithms have been developed for the retrieval of water constituents from the measurement of ocean color radiometry, and one of the approaches is spectral optimization. This approach defines an error target (or error function) between the input remote sensing reflectance and the output remote sensing reflectance, with the latter modeled with a few variables that represent the optically active properties (such as the absorption coefficient of phytoplankton and the backscattering coefficient of particles). The values of the variables when the error function reaches a minimum are the optimized properties that form the input remote sensing reflectance; or in other words, the equations of the model are solved numerically. The applications of this approach implicitly assume that the error is a monotonic function of the model variables before and after the minimization state is reached. Here, with data from numerical simulations, we show the shape of the error surface as a mechanism to visualize the solution space for the model variables. Further, using two established model forms as examples, we demonstrate how the solution space changes under different model assumptions as well as the impacts on the retrievals.

Keywords: ocean color remote sensing, optimization, algorithm

1. INTRODUCTION

The spectral distribution of reflected Sun light upwelling from beneath the ocean surface, which is often referred to as remote-sensing reflectance or $R_{rs}(\lambda)$, contains information on the composition of in-water constituents and forms the basis to retrieve such information from satellite measured radiance. Historically, the methods to quantitatively retrieve such information from ocean color radiometry include simple empirical regression techniques [1, 2], algebraic solutions [3, 4], and numerical optimization [5-8] of modeled spectrum based on inherent optical properties (IOP). One such spectral optimization algorithm (SOA) was proposed in the Coastal Zone Color Scanner (CZCS) era [5]. However, because it searches for the optimal set of solutions among numerous candidates for each measured reflectance spectrum, SOA was associated with large computational burden that consequently limited its application in processing satellite-measured ocean color images. In the recent decade, due to the rapid advancement of computer hardware and software, computation burden has become less critical and there is renewed interest in using SOA as an operational tool to process satellite ocean color data [9, 10] from modern sensors such as Sea-viewing Wide Field-of-view Sensor (SeaWiFS), Moderate Resolution Imaging Spectroradiometer (MODIS), and Medium Resolution Imaging Spectrometer (MERIS).

Various SOA schemes have been developed in the past three decades [11-13]. Two such algorithms include the Hyperspectral Optimization Process Exemplar (HOPE) model [6, 14] and the Garver-Siegel-Maritorena (GSM) model [15]. As with other published approaches [7, 12, 13], HOPE and GSM assume a spectral shape (or eigenvector) for the component IOPs (i.e., absorption due to phytoplankton and yellow substance, backscattering due to particles) and retrieve the optimal magnitudes (or eigenvalue) of those eigenvectors that best reproduce the spectral distribution of the observed ocean color signal. The principal differences between the models, therefore,

rest with the assumed spectral shapes of the component IOPs. The optimization schemes applied to these models assume that there is no local minimum in the error function or that any such local minimum can be overcome by the optimization algorithm and software [16, 17]. Here, using data from numerical simulations, we visualize the shape of the solution space and demonstrate that the error function has a clearly defined global minimum. More importantly, we show that the assumed spectral models have significant consequences on the closure between measured and modeled remote sensing reflectance and thus on retrievals of spectral optical properties.

2. BRIEF REVIEW OF SOA

For optically deep waters, the spectral reflectance upwelling from beneath the ocean surface, R_{rs} , can be modeled as a function of total absorption and total backscattering coefficients of the water column [18], i.e.,

$$R_{rs}(\lambda) = Fun(a(\lambda), B(\lambda)) \quad (1)$$

where $a(\lambda)$ and $B(\lambda)$ are the spectral absorption and backscattering coefficients, respectively.

For SOA, an error function is defined and minimized to derive the optimal model variables, i.e.,

$$\delta_{R_{rs}} = \frac{\sqrt{\overline{n_{\lambda_1}^{\lambda_2} (\bar{R}_{rs}(\lambda) - R_{rs}(\lambda))^2}}}{\overline{n_{\lambda_1}^{\lambda_2} R_{rs}(\lambda)}} = \sqrt{n} \frac{\sqrt{\sum_{\lambda_1}^{\lambda_2} (\bar{R}_{rs}(\lambda) - R_{rs}(\lambda))^2}}{\sum_{\lambda_1}^{\lambda_2} R_{rs}(\lambda)} \quad (2)$$

where $\overline{n_{\lambda_1}^{\lambda_2}}$ represents the average of a spectrum between wavelengths of λ_1 and λ_2 (n is the number of spectral bands), $R_{rs}(\lambda)$ is the spectrum from measurements, while $\bar{R}_{rs}(\lambda)$ is the spectrum from modeling.

Typically, $a(\lambda)$ and $B(\lambda)$ are modeled as spectral functions of a series of scalar variables X_i , with i generally equal to or greater than 3. $\bar{R}_{rs}(\lambda)$ then becomes a function of X_i , and $\delta_{R_{rs}}$ in general is:

$$\delta_{R_{rs}} = Fun(X_i) \quad (3)$$

In spectral optimization, for a given $R_{rs}(\lambda)$, the values of X_i are optimal when $\delta_{R_{rs}}$ reaches a minimum. For all SOA schemes, although there are subtle differences in handling the IOP to AOP model (Eq. 1) and the error function (Eq. 2), most of the differences are embedded in the spectral models of $a(\lambda)$ and $B(\lambda)$. For example, when the spectrum of particle backscattering is modeled as a power-law function of wavelength [1], the exponent value is 1.03 in the GSM [15], while it varies with $R_{rs}(\lambda)$ in HOPE [3]. Further, because of the different spectral models, different SOAs may have different $\delta_{R_{rs}}^{min}$ (minimized $\delta_{R_{rs}}$) (Figure 1a) or identical $\delta_{R_{rs}}^{min}$ but $\bar{R}_{rs}(\lambda)$ matches $R_{rs}(\lambda)$ at different wavelengths (Figure 1b). Because of such characterizations, SOA schemes are not the same, and the assumed spectral treatment of the $a(\lambda)$ and $B(\lambda)$ in individual SOA schemes is the primary driver for differences in remote-sensing retrievals (see examples in IOCCG Report #5 [11]).

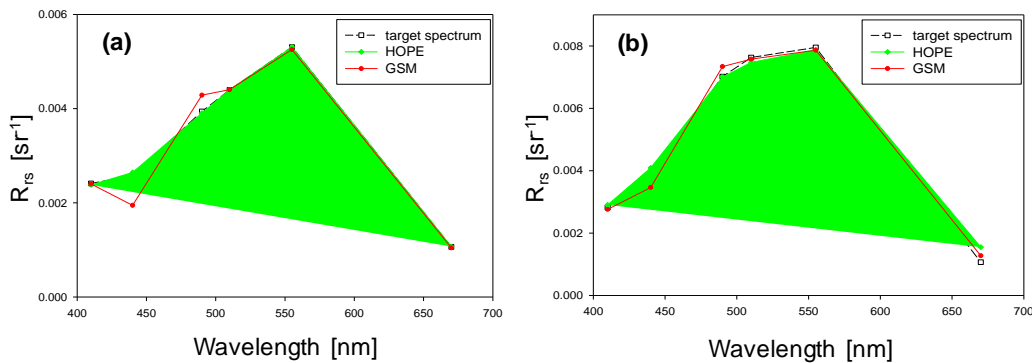


Figure 1. Examples of target and optimized spectral remote sensing reflectance. (a) HOPE and GSM achieved different degree of goodness of fit; (b) HOPE and GSM achieved identical goodness of fit, but the matching is different spectrally.

Compared with algebraic solutions, where all derivation steps are explicit, the solution steps of an SOA (i.e., numerical trial-and-error) are in general not explicit. To be able to have an unequivocal solution with an SOA scheme, $\delta_{R_{rs}}$ must have a global minimum, and the design of the computer software must be able to overcome local minima if they exist. It is therefore useful to know the surface shape of $\delta_{R_{rs}}$, especially around the value of $\delta_{R_{rs}}^{min}$.

For instance, if the surface shape of $\delta_{R_{rs}}$ resembles the letter U, i.e., it changes very slowly around $\delta_{R_{rs}}^{min}$ for changing X_i , it will result in either more computation time to reach $\delta_{R_{rs}}^{min}$ and/or ambiguity (large uncertainties) in the derived X_i values. On the other hand, if the surface shape of $\delta_{R_{rs}}$ resembles the letter V, i.e., it changes sharply around $\delta_{R_{rs}}^{min}$ for changing X_i , it will result in less computation time to reach $\delta_{R_{rs}}^{min}$ and less or no ambiguity in the derived X_i values.

3. DATA AND METHODS

3.1 Model of R_{rs}

Many studies were carried out in the past decades to find a suitable and accurate function to represent Eq. 1 (see review in Lee et al). Without loss of generality, and to be consistent with an earlier effort (GSM), here the model of Gordon et al [18] is used to calculate sub-surface remote-sensing reflectance (r_{rs}) from absorption and backscattering coefficients:

$$r_{rs} = \left(0.0949 + 0.0794 \frac{B}{a+B} \right) \frac{B}{a+B} \quad (4)$$

This r_{rs} is propagated through the surface to get the above-surface remote sensing reflectance (R_{rs})

$$R_{rs} = \frac{0.52 r_{rs}}{1 - 1.7 r_{rs}} \quad (5)$$

3.2 Data

The simulated dataset by the IOCCG Algorithm Working Group [11] is used in this study, which contains 500 spectral R_{rs} and the corresponding spectral IOP components, with wavelengths spanning the range of 400 – 800 nm at 10 nm spectral resolution. The dataset was sub-sampled to obtain wavelengths at 410, 440, 490, 510, 555, and 670 nm, spectral bands that closely match the settings of SeaWiFS. The values at 555 nm are simple averages of values at 550 nm and 560 nm. For each spectrally sub-sampled data point, $\tilde{R}_{rs}(\lambda)$ was calculated with $a(\lambda)$ and $B(\lambda)$ that were used as inputs for the Hydrolight simulations, and then $\delta_{R_{rs}}$ is calculated. Figure 2 shows the distributions of $\delta_{R_{rs}}$ of the 500 points when sub-sampled to SeaWiFS bands. Generally $\delta_{R_{rs}}$ is centered ~5%, which is consistent with the conclusion of Gordon et al [18] as the particle phase functions used in the IOCCG simulation and that in Gordon et al [18] are not identical. Note that in the inversion process (no matter which scheme), it is always considered that Eq. 4 is error free, so this model introduced difference will be propagated to the derived properties.

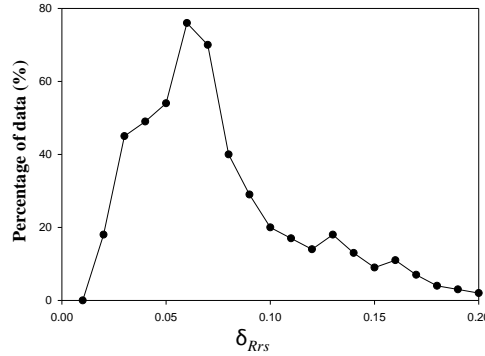


Figure 2. Distribution of “error” of Gordon et al [18] R_{rs} model.

3.3 Spectral model of IOPs

$\delta_{R_{rs}}$ is a complex function of X_i used to generate spectral R_{rs} . Let the number of variables as N and the number of spectral bands of R_{rs} as n (n has to be equal to or greater than N for possible solutions), $\delta_{R_{rs}}$ may reach 0 when n=N and increases with the value of (n-N) if R_{rs} is not spectrally correlated. For easier demonstrations and following a widely applied practice, we selected a three-parameter model system [19] to calculate $\tilde{R}_{rs}(\lambda)$. Basically, spectral $a(\lambda)$ and $B(\lambda)$ are modeled as

$$a(\lambda) = a_w(\lambda) + a_{ph}(\lambda) + a_{dg}(\lambda) \quad (6)$$

$$B(\lambda) = B_w(\lambda) + B_p(\lambda) \quad (7)$$

$a_w(\lambda)$ and $B_w(\lambda)$ are values of water molecules and are considered universal constants (although they may change slightly with temperature and salinity [20]), with $a_{ph}(\lambda)$, $a_{dg}(\lambda)$ and $B_p(\lambda)$ the absorption spectra of phytoplankton and detritus-gelbstoff and backscattering spectrum of suspended particles, respectively. Thus there are three unknown spectra ($a_{ph}(\lambda)$, $a_{dg}(\lambda)$ and $B_p(\lambda)$) in Eq. 5, and they are further modeled as

$$a_{ph}(\lambda) = X_1 \tilde{a}_{ph}(\lambda) \quad (8)$$

$$a_{dg}(\lambda) = X_2 \tilde{a}_{dg}(\lambda) \quad (9)$$

$$B_p(\lambda) = X_3 \tilde{B}_p(\lambda) \quad (10)$$

$X_{1,3}$ are the three scalar variables to be derived from a measured R_{rs} via SOA. $\tilde{a}_{ph}(\lambda)$, $\tilde{a}_{dg}(\lambda)$ and $\tilde{B}_p(\lambda)$ are spectral models (eigenvectors) determined based on either field measurements [7, 8, 21, 22] or “optimized” from a database [15].

In general, $\tilde{a}_{dg}(\lambda)$ and $\tilde{B}_p(\lambda)$ can be described as [1, 23]:

$$\tilde{a}_{dg}(\lambda) = e^{-S(\lambda-\lambda_0)} \quad (11)$$

$$\tilde{B}_p(\lambda) = \left(\frac{\lambda_0}{\lambda}\right)^Y \quad (12)$$

The spectral slope (S) of $\tilde{a}_{dg}(\lambda)$ and the power coefficient (Y) are not constants for global waters. To reduce variables, S is set as 0.015 nm^{-1} in HOPE, but 0.0206 nm^{-1} in GSM; while Y changes with R_{rs} in HOPE, but is fixed as 1.03 in GSM. The reference wavelength (λ_0) is generally set as 440 nm.

It is much more difficult to precisely model spectral $\tilde{a}_{ph}(\lambda)$ [13, 22, 24, 25], although better fits could be achieved by increasing the number of free variables. As an example, we selected two simple models (where $a_{ph}(\lambda)$ is modeled with one variable) to evaluate their impacts: one is the $\tilde{a}_{ph}(\lambda)$ in HOPE, for which the spectral shape varies with the value of $a_{ph}(440)$ (which is equivalent to chlorophyll concentration); and one is the $\tilde{a}_{ph}(\lambda)$ in GSM, which is constant for global waters. Figure 3 shows examples of the $\tilde{a}_{ph}(\lambda)$ for various eutrophication states, and the following provides a mathematic expression of the two approaches:

HOPE:

$$\tilde{a}_{ph}(\lambda) = a_0(\lambda) + a_1(\lambda) \ln(P) \quad (13)$$

GSM:

$$\tilde{a}_{ph}(\lambda) = A_{ph-GSM}(\lambda) \quad (14)$$

Using SeaWiFS band setup as an example, there are R_{rs} data at 6 bands (411, 443, 490, 510, 555, and 670 nm) that are generally useful for remote sensing retrieval of in-water constituents. Data at the longer wavelengths are used for atmospheric corrections.

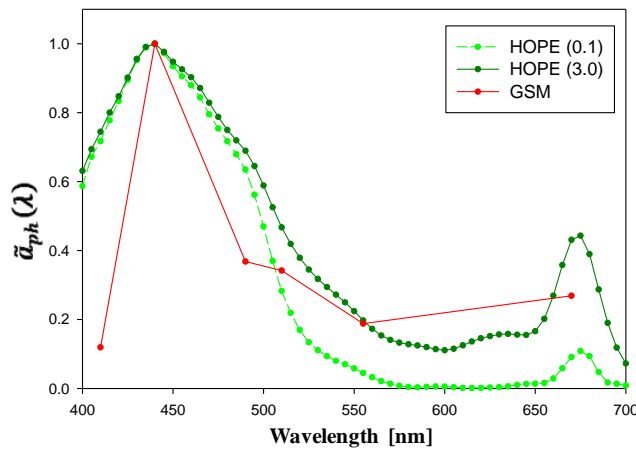


Figure 3. Comparison of the a_{ph} spectral shapes used in HOPE and GSM. #'s in the parenthesis indicate likely concentration of chlorophyll.

3.4 Optimization setups and software

For all numerical solutions, a set of initial values (first guess) is required to start the process. In HOPE, the initial values of the three variables are not kept constant, but are estimated for each given $R_{rs}(\lambda)$ as follow:

$$X_1 = 0.05 \left(\frac{R_{rs}(440)}{R_{rs}(555)} \right)^{-1.5} \quad (15)$$

$$X_2 = X_1 \quad (16)$$

$$X_3 = 20 (0.06 + 0.3 X_1) R_{rs}(555) \quad (17)$$

Note that X_I represents $a_{ph}(440)$ in HOPE. For GSM, the same starting values are used, but in this case X_I represents Chl, so $a_{ph}(440)$ is converted to Chl following Eq. 8 by dividing the corresponding chlorophyll-specific value ($a_{ph}^*(440)$) at 440 nm.

To generate physically meaningful solutions, boundaries of the three variables have to be set up, and they are (for HOPE):

$$0.002 \leq X_1 \leq 1.0 \text{ m}^{-1};$$

$$0.002 \leq X_2 \leq 5.0 \text{ m}^{-1};$$

$$0.0001 \leq X_3 \leq 0.5 \text{ m}^{-1}.$$

When using the $a_{ph}(\lambda)$ model of GSM, while the boundaries for X_2 and X_3 are kept the same, X_1 (for Chl) is set as

$$0.02 \leq X_1 \leq 100 \text{ mg m}^{-3}.$$

To derive the 3 scalar variables for each R_{rs} , we used the Solver tool included in MS Excel. This tool uses several algorithms to find optimal solutions that include the Generalized Reduced Gradient Nonlinear Solving Method developed by Lasdon et al [26] and the Simplex LP Solving Method implemented by Fylstra et al [27].

After the optimization is reached for each $R_{rs}(\lambda)$, we not only recorded the δ_{RRS}^{min} (the global minimum of δ_{RRS}), but also the difference between the derived spectral IOPs and the known spectral IOPs, which is calculated using Eq. 2, except that $\tilde{R}_{rs}(\lambda)$ is replaced by the spectral IOPs that formed the optimized $\tilde{R}_{rs}(\lambda)$, and $R_{rs}(\lambda)$ is replaced by the corresponding known spectral IOPs. We calculated δ_a (for total absorption coefficient), δ_{Bp} (for particle backscattering coefficient), δ_{aph} (for phytoplankton absorption coefficient), and δ_{adg} (for CDOM/gelbstoff coefficient), respectively. The wavelength range for these IOPs are from 410 nm to 555 nm, as there is limited information that can be derived in the longer wavelengths for most oceanic waters. These δ_{IOP} values provide a measure of the goodness of the derived spectral inherent optical properties.

4. RESULTS AND DISCUSSIONS

The surface shape of δ_{RRS} provides an indicator of the effectiveness of an SOA approach. For the spectral IOP models evaluated here, examples of the surface shapes are presented in Figure 4, while the overall distributions of δ_{RRS}^{min} are shown in Figure 5.

4.1 δ_{RRS} surface

Figure 4 shows examples of δ_{RRS} (expressed as the percentage change of δ_{RRS} in relation to the percentage of change of a_{ph} , a_{dg} , and B_p) of both HOPE and GSM models. Generally, δ_{RRS} is monotonic in relation to X_i before and after δ_{RRS} reaches its global minimum. To understand the shape of δ_{RRS} , consider a simplified R_{rs} model where the total backscattering and total absorption spectra are modeled as one variable, respectively, then the model of remote sensing reflectance can be simplified as

$$\tilde{R}_{rs}(\lambda) = A(\lambda) \frac{B'_w(\lambda) + B_{nw}}{a'_w(\lambda) + a_{nw}} \quad (18)$$

Here, $B'_w(\lambda)$ and $a'_w(\lambda)$ are spectra associated with the backscattering and absorption coefficients of pure seawater, respectively, and are considered as constant; and B_{nw} and a_{nw} are two scalar variables for the backscattering and absorption coefficients of non-water constituents, respectively. $A(\lambda)$ represents a combination of the spectral shapes of the two components and is constant for a given $R_{rs}(\lambda)$.

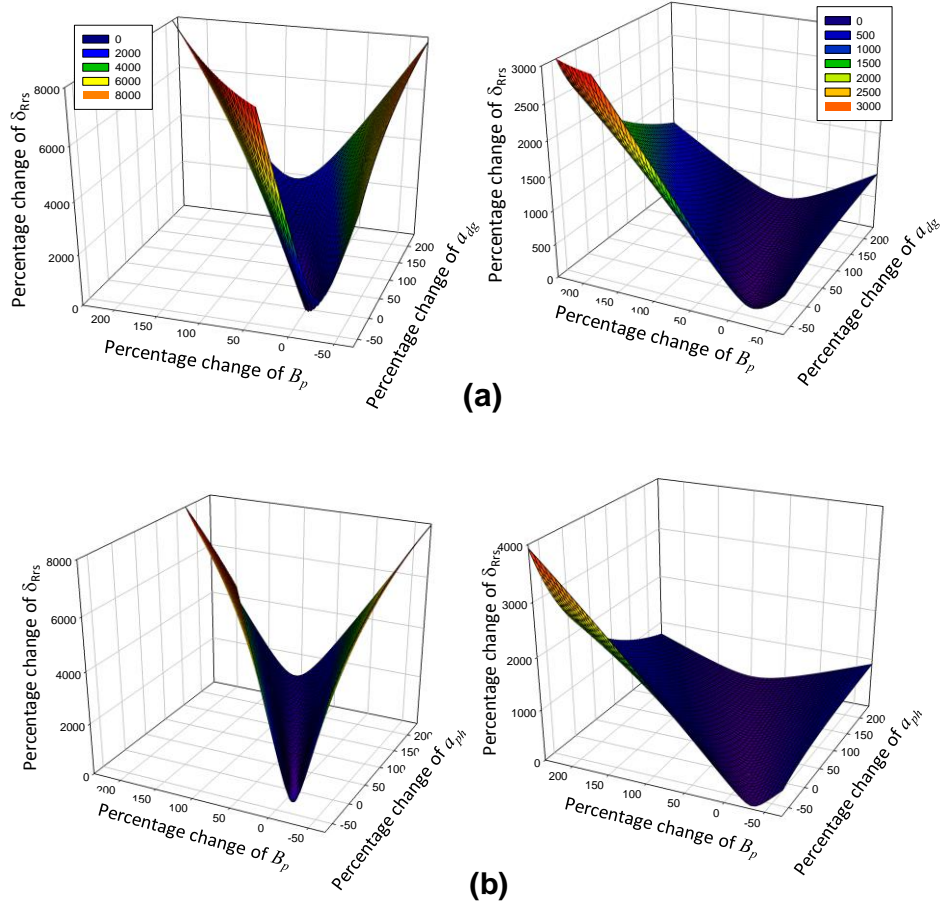


Figure 4. (a) Examples of surface shape of δ_{Rrs} resulted from change of B_p and a_{dg} . (left) HOPE; (right) GSM; (b) Examples of surface shape of δ_{Rrs} resulted from change of B_p and a_{ph} . (left) HOPE; (right) GSM.

With such a simplified model, we examine the variation of R_{rs} resulting from the change of B_{nw} and a_{nw} . Note that, since the denominator of Eq. 2 is a fixed value for a given $R_{rs}(\lambda)$ (does not change with X_i), the SOA is optimal when the following error-measure reaches a minimum,

$$\Delta_{Rrs} = \sum_{\lambda 1}^{\lambda 2} \left(\tilde{R}_{rs}(\lambda) - R_{rs}(\lambda) \right)^2 \quad (19)$$

And, Δ_{Rrs} changes with B_{nw} through

$$\frac{\partial \Delta_{Rrs}}{\partial B_{nw}} = 2 \sum_{\lambda 1}^{\lambda 2} \left(A(\lambda) \frac{B_w(\lambda) + B_{nw}}{a_w(\lambda) + a_{nw}} - R_{rs}(\lambda) \right) \frac{A(\lambda)}{a_w(\lambda) + a_{nw}} \quad (20)$$

while Δ_{Rrs} changes with a_{nw} through

$$\frac{\partial \Delta_{Rrs}}{\partial a_{nw}} = -2 \sum_{\lambda 1}^{\lambda 2} \left(A(\lambda) \frac{B_w(\lambda) + B_{nw}}{a_w(\lambda) + a_{nw}} - R_{rs}(\lambda) \right) A(\lambda) \frac{B_w(\lambda) + B_{nw}}{(a_w(\lambda) + a_{nw})^2} \quad (21)$$

For a given a_{nw} , there is a value of B_{nw} that makes $\frac{\partial \Delta_{Rrs}}{\partial B_{nw}}$ equal to zero (same for a_{nw}). When optimization is reached, both $\frac{\partial \Delta_{Rrs}}{\partial B_{nw}}$ and $\frac{\partial \Delta_{Rrs}}{\partial a_{nw}}$ reach zero. Furthermore, $\frac{\partial \Delta_{Rrs}}{\partial B_{nw}}$ is negative (negative slope) when B_{nw} is smaller than the optimized B_{nw} value, and Δ_{Rrs} decreases with the increase of B_{nw} toward the optimum value; similarly, $\frac{\partial \Delta_{Rrs}}{\partial B_{nw}}$ is positive (positive slope) when B_{nw} is larger than the optimized B_{nw} value, and Δ_{Rrs} increases with the increase of B_{nw} away from the optimum value. This monotonic behavior on either side of the global minimum just illustrates that there is no local minimum.

If a_{nw} (or B_{nw}) is modeled with two or more components (e.g., Eq. 13), the variation of Δ_{Rrs} for each individual component becomes more complex. In particular, it will depend on whether the two (or more) components are spectrally distinguishable enough, otherwise the solution for these components will not be unique and thus the separation cannot be resolved (such as the separation of absorption between detritus and gelbstoff). Fortunately, the spectral shapes between a_{ph} and a_{dg} are significantly different in the 410 – 670 nm range, which ensures a general resolution of these two components, although uncertainty of each derived component varies case by case [28] and the impact on both $\frac{\partial \delta_{Rrs}}{\partial a_{dg}}$ and $\frac{\partial \delta_{Rrs}}{\partial a_{ph}}$ is strong (see Figure 4).

4.2 δ_{Rrs}^{min} distribution

The spectral models for IOPs not only affect the shape of the error function, but also the value of δ_{Rrs}^{min} (a measure of closure). Figure 5a presents the δ_{Rrs}^{min} values from both HOPE and GSM models for the 500 simulated data, respectively, and Figure 5b shows the distribution of the δ_{Rrs}^{min} values. The X-axis of Figure 5a is roughly arranged in order from low-complexity, oligotrophic waters ($a(440) \sim 0.016 \text{ m}^{-1}$) to higher-complexity, eutrophic waters ($a(440) \sim 3.2 \text{ m}^{-1}$). Generally, δ_{Rrs}^{min} from the HOPE model is smaller than that from the GSM model (δ_{Rrs}^{min} is centered around 0.03 for HOPE while it spans between 0.04 and 0.10 for GSM). The δ_{Rrs}^{min} value from the HOPE model increases with the complexity of the water, which is expected because, for eutrophic waters, it is less likely that the assumed $\tilde{a}_{ph}(\lambda)$ matches perfectly the actual phytoplankton absorption spectrum. However, it is interesting and intriguing that the δ_{Rrs}^{min} value of GSM increases then decreases with the increasing of complexity.

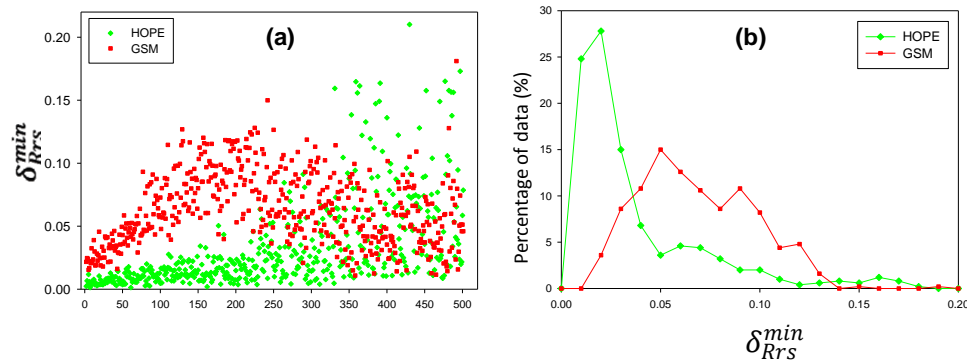


Figure 5. Values and distributions of δ_{Rrs}^{min} from HOPE and GSM.

4.3 δ_{IOP} distribution

After optimization was achieved, the derived spectral models of the IOPs were compared with the known IOP inputs used to generate the simulated R_{rs} spectra to measure the quality of the SOA retrievals. Different from the usual evaluation of retrieved IOPs at a single wavelength, the scheme here basically considers the IOP spectrum as a whole and evaluates this spectrum. This is valuable because that both the quantity and quality of the sub-surface light field is determined by the IOP spectra. Figures 6-9 present the values of δ_{IOP} (spectra of total absorption, phytoplankton absorption, detritus-gelbstoff absorption, and particle backscattering, respectively) obtained from both HOPE and GSM. δ_{IOP} is calculated following Eq. 2, but restricting the wavelength range to 410-555 nm, as the longer wavelength (670 nm here) has limited information of the active optical components. A few general points are observed for this dataset:

- δ_{IOP} of HOPE is smaller than that of GSM
- For absorption spectrum, mean δ_a is $\sim 8\%$ and smaller for low complexity (blue) waters (Figure 6) when HOPE is used
- δ_{aph} and δ_{adg} are much higher than δ_a , and δ_{aph} of GSM is much higher than that of HOPE. This is probably because the $\tilde{a}_{ph}(\lambda)$ used in GSM not well represent the spectral shape observed from sample measurements
- δ_{Bp} of HOPE is centered $\sim 10\%$ while δ_{Bp} from GSM spans a range of $\sim 10\text{-}50\%$. Again, δ_{Bp} from HOPE increases with increasing complexity, but δ_{Bp} from GSM slightly decreases then increases with water complexity.

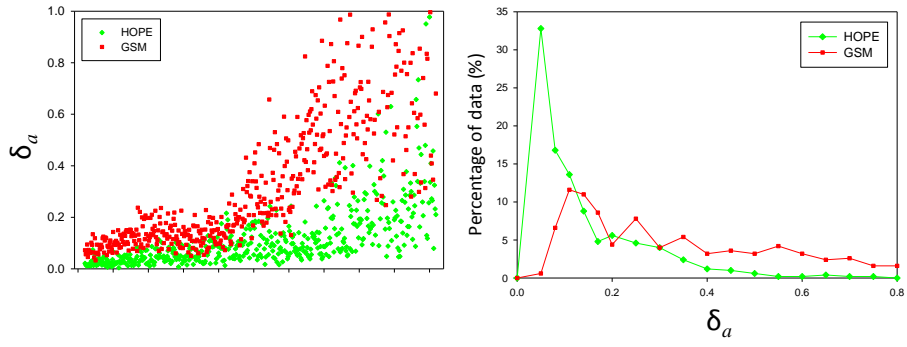


Figure 6. Values and distributions of δ_a .

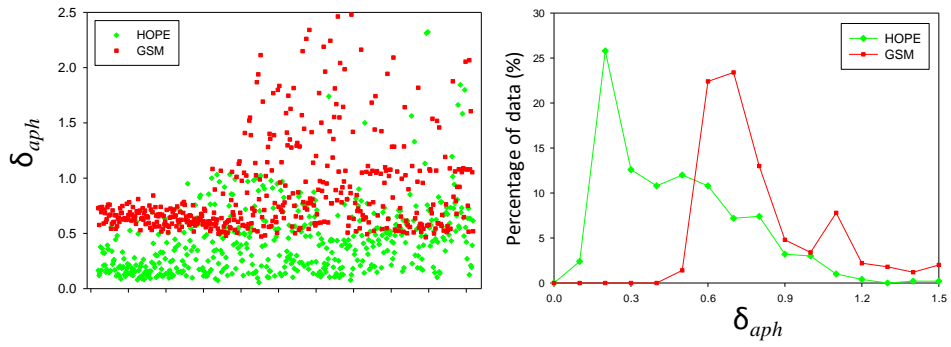


Figure 7. Values and distributions of δ_{apl} .

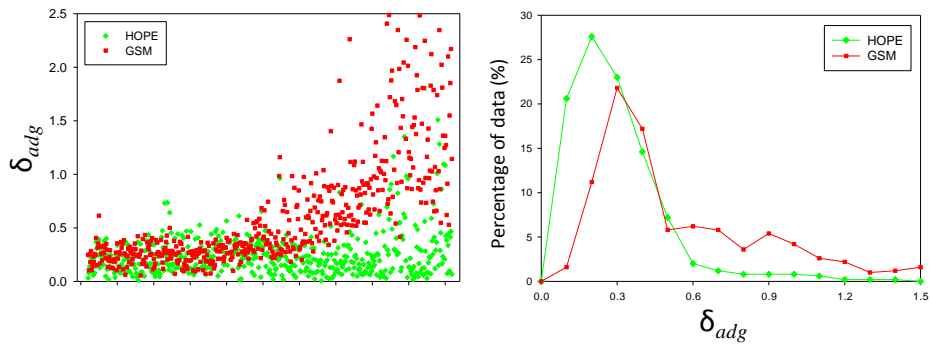


Figure 8. Values and distributions of δ_{adg} .

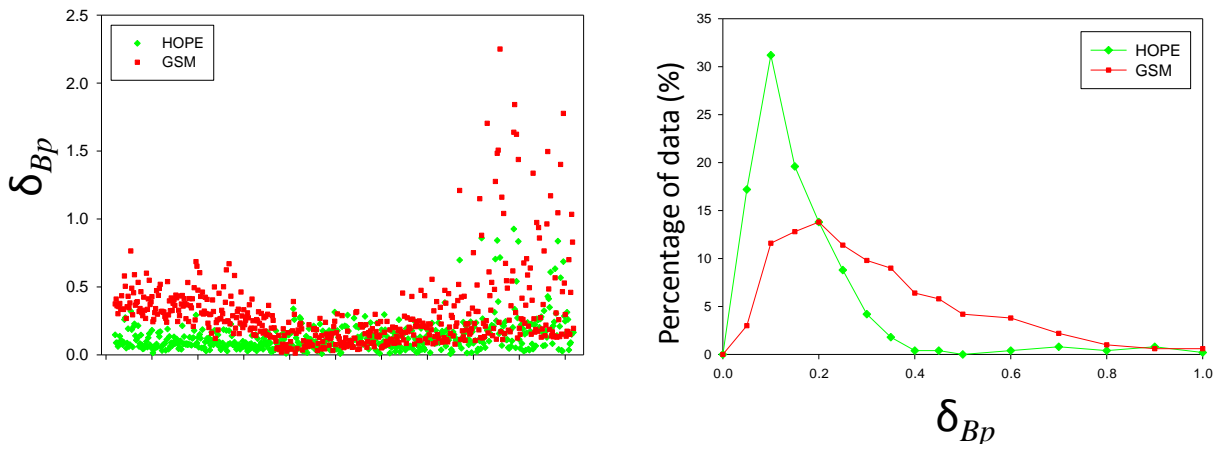


Figure 9. Values and distributions of δ_{Bp} .

5. SUMMARY

With a simplified model for remote sensing reflectance, we proved that the error function used to measure the goodness-of-fit is in general a monotonic function of backscattering and absorption before and after the optimization point (especially for blue waters with a spectral range of 400-700 nm). It is not possible for the SOA solution of such model to become trapped in a local minimum before reaching the global minimum. However, this ultimately depends on other factors such as the complexity of the models and water properties and the spectral range and resolution of the observed spectral R_{rs} . Further, we applied two spectral optimization algorithms (HOPE and GSM) to the IOCCG numerically simulated data and showed how the different model assumptions affect the closure between modeled and known R_{rs} , the surface shape of the error function, and the quality of SOA retrieved spectral IOPs. Results here further highlight the necessity and importance to develop and utilize appropriate models for the spectral shape of the IOPs for SOA schemes.

ACKNOWLEDGEMENT

Financial support for this study was provided by NASA and NRL.

REFERENCE

1. Gordon, H.R. and A. Morel, *Remote assessment of ocean color for interpretation of satellite visible imagery: A review*. 1983, New York: Springer-Verlag. 44.
2. O'Reilly, J., et al., *Ocean color chlorophyll algorithms for SeaWiFS*. J. Geophys. Res., 1998. **103**: p. 24937-24953.
3. Lee, Z.P., K.L. Carder, and R. Arnone, *Deriving inherent optical properties from water color: A multi-band quasi-analytical algorithm for optically deep waters*. Applied Optics, 2002. **41**: p. 5755-5772.
4. Smyth, T.J., et al., *Semianalytical model for the derivation of ocean color inherent optical properties: description, implementation, and performance assessment*. Appl. Opt., 2006. **45**(31): p. 8116-8131.
5. Doerffer, R. and J. Fisher, *Concentrations of chlorophyll, suspended matter, and gelbstoff in case II waters derived from satellite coastal zone color scanner data with inverse modeling methods*. J. Geophys. Res., 1994. **99**: p. 7475-7466.
6. Lee, Z.P., *Visible-infrared Remote-sensing Model and Applications for Ocean Waters*, in *Department of Marine Science*. 1994, The University of South Florida: St. Petersburg. p. 160.
7. Bukata, R.P., et al., *Optical Properties and Remote Sensing of Inland and Coastal Waters*. 1995, Boca Raton, FL: CRC Press.
8. Roesler, C.S. and M.J. Perry, *In situ phytoplankton absorption, fluorescence emission, and particulate backscattering spectra determined from reflectance*. J. Geophys. Res., 1995. **100**: p. 13279-13294.
9. Hu, C., et al. *Application of an optimization algorithm to satellite ocean color imagery: A case study in Southwest Florida coastal waters*. in *Ocean Remote Sensing and Applications*. 2002. Hangzhou, China: SPIE.
10. Werdell, P.J., *Global bio-optical algorithms for ocean color satellite applications*. AGU EOS Transactions 2009. **90**(1): p. doi:10.1029/2009EO010005.
11. IOCCG, *Remote Sensing of Inherent Optical Properties: Fundamentals, Tests of Algorithms, and Applications*, in *Reports of the International Ocean-Colour Coordinating Group, No. 5*, Z.-P. Lee, Editor. 2006, IOCCG: Dartmouth, Canada. p. 126.
12. Brando, V.E. and A.G. Dekker, *Satellite hyperspectral remote sensing for estimating estuarine and coastal water quality*. IEEE Transactions on Geoscience and Remote Sensing, 2003. **41**(6): p. 1378-1387.
13. Devred, E., et al., *A two-component model of phytoplankton absorption in the open ocean: Theory and applications*. J. Geophys. Res., 2006. **111**: p. C03011, doi:10.1029/2005JC002880.
14. Lee, Z.P., et al., *Hyperspectral remote sensing for shallow waters: 2. Deriving bottom depths and water properties by optimization*. Applied Optics, 1999. **38**: p. 3831-3843.
15. Maritorena, S., D.A. Siegel, and A.R. Peterson, *Optimization of a semianalytical ocean color model for global-scale applications*. Applied Optics, 2002. **41**: p. 2705-2714.
16. Chami, M. and D. Robilliard, *Inversion of Oceanic Constituents in Case I and II Waters with Genetic Programming Algorithms*. Applied Optics, 2002. **41**(30): p. 6260-6275.
17. Liu, C.-C., C.-H. Chang, and C.-G. Wen, *Integrating semianalytical and genetic algorithms to retrieve the constituents of water bodies from remote sensing of ocean color*. Optical Express, 2007. **15**(2): p. 252-265.
18. Gordon, H.R., et al., *A semianalytic radiance model of ocean color*. J. Geophys. Res., 1988. **93**: p. 10,909-10,924.

19. Sathyendranath, S., L. Prieur, and A. Morel, *A three-component model of ocean colour and its application to remote sensing of phytoplankton pigments in coastal waters*. Int. J. Remote Sensing, 1989. **10**: p. 1373-1394.
20. Pegau, W.S., D. Gray, and J.R.V. Zaneveld, *Absorption and attenuation of visible and near-infrared light in water: dependence on temperature and salinity*. Applied Optics, 1997. **36**(24): p. 6035-6046.
21. Lee, Z.P., et al., *Hyperspectral remote sensing for shallow waters. 1. A semianalytical model*. Applied Optics, 1998. **37**: p. 6329-6338.
22. Bricaud, A., et al., *Variability in the chlorophyll-specific absorption coefficients of natural phytoplankton: Analysis and parameterization*. J. Geophys. Res., 1995. **100**: p. 13321-13332.
23. Bricaud, A., A. Morel, and L. Prieur, *Absorption by dissolved organic matter of the sea (yellow substance) in the UV and visible domains*. Limnol. Oceanogr., 1981. **26**: p. 43-53.
24. Bricaud, A. and D. Stramski, *Spectral absorption coefficients of living phytoplankton and nonalgal biogenous matter: A comparison between the Peru upwelling area and the Sargasso Sea*. Limnol. Oceanogr., 1990. **35**: p. 562-582.
25. Ciotti, A.M., M.R. Lewis, and J.J. Cullen, *Assessment of the relationships between dominant cell size in natural phytoplankton communities and spectral shape of the absorption coefficient*. Limnol. Oceanogr., 2002. **47**: p. 404-417.
26. Lasdon, L.S., et al., *Design and testing of generalized reduced gradient code for nonlinear programming*. 1976: Stanford CA. p. 51.
27. Fylstra, D., et al., *Design and Use of the Microsoft Excel Solver*. INTERFACES, 1998. **28**(5): p. 29-55.
28. Lee, Z., et al., *Uncertainties of optical parameters and their propagations in an analytical ocean color inversion algorithm*. Applied Optics, 2010. **49**(3): p. 369-381.